

MASSIVE MOLECULAR GAS RESERVOIR IN A LUMINOUS SUB-MILLIMETER GALAXY DURING COSMIC NOON

BIN LIU,^{1,2} N. CHARTAB,² H. NAYYERI,² A. COORAY,² C. YANG,^{3,4} D.A. RIECHERS,⁵ M. GURWELL,⁶ ZONG-HONG ZHU,^{1,7} S. SERJEANT,⁸ E. BORSATO,⁹ M. NEGRELLO,¹⁰ L. MARCHETTI,^{11,12,13} E.M. CORSINI,^{9,14} AND P. VAN DER WERF¹⁵

¹*Department of Astronomy, Beijing Normal University, Beijing 100875, China*

²*Department of Physics and Astronomy, University of California, Irvine, CA92697, USA*

³*Joint ALMA Observatory, Alonso de Córdova 3107, Vitacura 763-0355, Santiago, Chile*

⁴*European Southern Observatory, Alonso de Córdova 3107, Vitacura, Casilla 19001, Santiago de Chile, Chile*

⁵*Cornell University, Space Sciences Building, Ithaca, NY 14853, USA*

⁶*Center for Astrophysics | Harvard & Smithsonian, 60 Garden Street, Cambridge, MA 02138, USA*

⁷*School of Physics and Technology, Wuhan University, Wuhan 430072, China*

⁸*School of Physical Sciences, The Open University, Milton Keynes, MK7 6AA, UK*

⁹*Dipartimento di Fisica e Astronomia ‘G. Galilei’, Università di Padova, Vicolo dell’Osservatorio 3, 35122, Padova, Italy*

¹⁰*School of Physics and Astronomy, Cardiff University, The Parade, Cardiff, CF24 3AA, UK*

¹¹*School of Physical Sciences, The Open University, Milton Keynes MK7 6AA, UK*

¹²*Department of Astronomy, University of Cape Town, Private Bag X3, Rondebosch, 7701 Cape Town, South Africa*

¹³*INAF - Istituto di Radioastronomia, via Gobetti 101, I-40129 Bologna, Italy*

¹⁴*INAF - Osservatorio Astronomico di Padova, vicolo dell’Osservatorio 5, I-35122 Padova, Italy*

¹⁵*Leiden University, Leiden Observatory, PO Box 9513, NL-2300 RA, Leiden, The Netherlands*

ABSTRACT

We present multi-band observations of an extremely dusty star-forming lensed galaxy (HERS1) at $z = 2.553$. High-resolution maps of *HST*/WFC3, SMA, and ALMA show a partial Einstein ring with a radius of $\sim 3''$. The deeper HST observations also show the presence of a lensing arc feature associated with a second lens source, identified to be at the same redshift as the bright arc based on a detection of the [NII] $205\mu\text{m}$ emission line with ALMA. A detailed model of the lensing system is constructed using the high-resolution HST/WFC3 image, which allows us to study the source plane properties and connect rest-frame optical emission with properties of the galaxy as seen in sub-millimeter and millimeter wavelengths. Corrected for lensing magnification, the spectral energy distribution fitting results yield an intrinsic star formation rate of about $1000 \pm 260 \text{ M}_{\odot}\text{yr}^{-1}$, a stellar mass $M_{*} = 4.3_{-1.0}^{+2.2} \times 10^{11} \text{ M}_{\odot}$, and a dust temperature $T_d = 35_{-1}^{+2} \text{ K}$. The intrinsic CO emission line ($J_{\text{up}} = 3, 4, 5, 6, 7, 9$) flux densities and CO spectral line energy distribution are derived based on the velocity-dependent magnification factors. We apply a radiative transfer model using the large velocity gradient method with two excitation components to study the gas properties. The low-excitation component has a gas density $n_{\text{H}_2} = 10^{3.1 \pm 0.6} \text{ cm}^{-3}$ and kinetic temperature $T_k = 19_{-5}^{+7} \text{ K}$ and a high-excitation component has $n_{\text{H}_2} = 10^{2.8 \pm 0.3} \text{ cm}^{-3}$ and $T_k = 550_{-220}^{+260} \text{ K}$. Additionally, HERS1 has a gas fraction of about 0.4 ± 0.2 and is expected to last 250 Myr. These properties offer a detailed view of a typical sub-millimeter galaxy during the peak epoch of star-formation activity.

Keywords: Gravitational lensing: strong – Submillimeter: galaxies – Galaxy: formation

1. INTRODUCTION

The cold molecular gas (traced by mm observations of the molecular CO) is the key fuel for active star formation in galaxies (Carilli & Walter 2013). The fraction of the molecular gas reservoir that ends up in new stars (what is usually referred to as the star formation efficiency) depends on parameters such as the fragmentation and chemical compositions of the gas and is diminished by phenomena that disperse the gas and

prevent the collapse, such as feedback from an active nucleus (AGN) or star-formation driven winds (Bigiel et al. 2008; Sturm et al. 2011; Swinbank et al. 2011; Fu et al. 2012). Existing evidence suggests AGN activity is the dominant mechanism in quenching star-formation at high redshifts, specifically in the most extreme environments (Cicone et al. 2014). On the other hand, the UV emission from newly born hot stars in star-forming regions ionizes the surrounding gas generating a wealth

of recombination nebular emission lines. The presence and intensity of these lines reveal valuable information on the physics of ionized gas surrounding these regions (Kriek et al. 2015; Shapley et al. 2015; Coil et al. 2015).

The most intense sites of star-formation activities in the universe at high redshift happen in the gas-rich dusty star forming galaxies (Casey et al. 2014). These heavily dust obscured systems are often discovered in the millimeter wavelengths and are believed to be the progenitors of the most massive red galaxies found at lower redshifts (Toft et al. 2014). Despite many efforts, the physics of the ionized gas (chemical composition, spatial extent and relative line abundance) is still poorly understood for these star-forming factories of the universe. Recent resolved studies of ionized gas at high redshift mostly focus on normal star-forming galaxies and miss this hidden population of starbursting systems (Genzel et al. 2011; Förster Schreiber et al. 2014).

The sub-millimeter galaxies (SMGs) are more efficient in turning gas into stars than normal star-forming galaxies at the same epoch (i.e., LBGs and BzK -selected galaxies), similar to local ultraluminous infrared galaxies (ULIRGs) (Negrello et al. 2007, 2010). Recent studies suggest that the LBG selected star forming galaxies might be fundamentally different from that of the SMGs whereas the former is usually characterized by $\text{SFR} < 100 \text{ M}_{\odot} \text{ yr}^{-1}$ the latter dominates the high SFR end and these are believed to be driven by different star formation mechanisms (Casey 2016). Using un-lensed SMGs, Menéndez-Delmestre et al. (2013) showed that star formation scale in these high redshift systems seems to be very different from that of local starburst and are more extended over 2-3 kpc scales.

Through *Herschel* wide-area surveys, we have now identified hundreds of extremely bright sub-millimeter sources ($S_{500\mu\text{m}} \geq 100 \text{ mJy}$) at high redshifts. After removing nearby contaminants, such bright $500 \mu\text{m}$ sources are either gravitationally lensed SMGs or multiple SMGs blended within the $18''$ *Herschel* PSF (Negrello et al. 2007, 2010, 2017) with most turning out to be strongly lensed SMGs in our high-resolution follow-up observations (Wardlow et al. 2013; Fu et al. 2012; Timmons et al. 2015). For this study we have selected a very bright Keck/NIRC2 observed Einstein ring lensed SMG at $z = 2.553$ (HERS J020941.1+001557 designated as HERS1 hereafter; Figure 1). This target is identified from the *Herschel* Stripe 82 survey (Viero et al. 2014) covering 81 deg^2 with *Herschel*/SPIRE instrument at 250, 350, and $500 \mu\text{m}$. HERS1 at $z=2.553$ is the brightest galaxy in *Herschel* extra-galactic maps with $S_{500\mu\text{m}} = 717 \pm 8 \text{ mJy}$. The galaxy was first identified as a gravitationally lensed radio source by two fore-

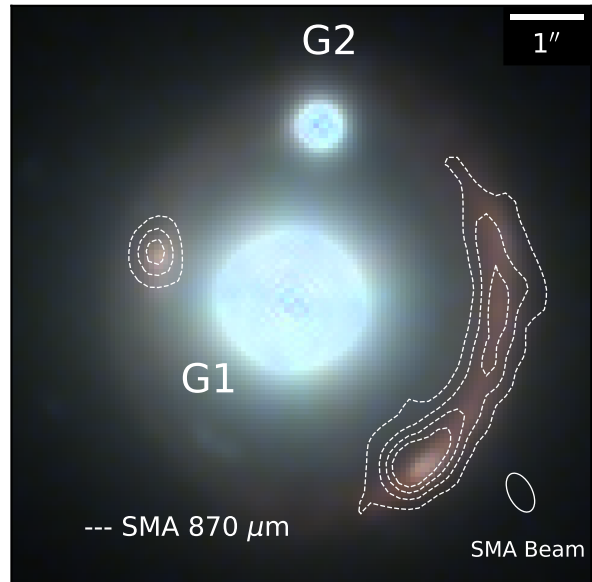


Figure 1. Three-color image of HERS1 adopting HST/WFC3 F110W (blue), F125W (green) and F160W (red) with sub-millimeter array (SMA) $870 \mu\text{m}$ contours overlaid. The SMA contours start from 9σ and increase in steps of 9σ with $\sigma = 305 \mu\text{Jy beam}^{-1}$. The beam size is shown in the bottom right. Two deflecting galaxies at $z=0.202$ (Geach et al. 2015) are marked as G1 and G2.

ground galaxies at $z = 0.202$ in a citizen science project (Geach et al. 2015) to an Einstein-ring with a radius $\sim 3''$. HERS1 has also been selected by other wide-area surveys such as *Planck*, ACT and has extensive follow-up observations from CFHT and HST in the near infrared along with ancillary observations by JVL, SCUBA-2 and ALMA with a CO redshift from Redshift Search Receiver of LMT and independently from $\text{H}\alpha$ using the IRCS on Subaru (Geach et al. 2015; Harrington et al. 2016; Su et al. 2017). Here we report new data from Keck/NIRC2 Laser Guide Star Adaptive Optics (LGS-AO) imaging in H and K_s bands, HST/WFC3 F125W, Sub-millimeter Array (SMA), and ALMA. The wealth of multi-band data combined with high resolution deep imaging provide a unique opportunity to study physical properties of HERS1 as an extremely bright sub-millimeter galaxy during the peak epoch of star formation activity.

This paper is organized as follows: In Section 2 we present observations and data reduction as well as previous archival data. In Section 3, we describe the lens modeling procedures and reconstructed source plane images of the high-resolution observations. We then show the source properties including CO spectral line energy distribution (SLED), de-lensed CO spectral lines, large

velocity gradient (LVG) modelling as well as infrared spectral energy distribution (SED) fitting in Section 4. Finally, we summarize our results in Section 5.

Throughout this paper, we assume a standard flat- Λ CDM cosmological model with $H_0 = 70 \text{ km s}^{-1} \text{ Mpc}^{-1}$ and $\Omega_\Lambda = 0.7$. All magnitudes are in the AB system.

2. DATA

2.1. Hubble Space Telescope WFC3 Imaging

HERS1 was observed on 2018 September 02 under GO program 15475 in Cycle 25 with two orbits (PI: Nayyeri). We used WFC3 F125W filter with a total exposure time of 5524s. The data were reduced by HST pipeline resulting a pixel scale of 0.128 arcsec. The photometry was performed following the WFC3 handbook.

2.2. Keck Near-IR Imaging

The near-IR data of HERS1 was observed with the KECK/NIRC2 Adaptive Optics system on 2017 August 27 (PID: U146; PI: Cooray). The H and K_s band filters were used at $1.60 \mu\text{m}$ and $2.15 \mu\text{m}$ respectively. The observations were done with a custom nine-point dithering pattern for sky subtraction with 120s (H band) and 80s (K_s band) exposures per frame. Each frame has a scale of 0.04 arcsec per pixel adopting the wide camera in imaging mode. The data were reduced by a custom IDL routine (Fu et al. 2012).

2.3. Sub-millimeter Array

Observations of HERS1 were obtained in three separate configurations of the SMA as described below. In each configuration, observations of HERS1 were obtained in tracks shared with a second target. Generally, seven of the eight SMA antennas participated in the observations, except in one case (see below). The SMA operates in double sideband mode, with sideband separation handled through a standard phase-switching procedure within the correlator (Ho et al. 2004). During the period, the new SMA SWARM correlator was expanding, resulting in increasing continuum bandwidth with each observation. All observations were obtained with a mean frequency between 341 and 343 GHz ($870 \mu\text{m}$).

HERS1 was first observed in the SMA subcompact configuration (maximum baselines 45 m) on 2016 September 20 (PID: 2016A-S007; PI: Cooray). The weather was good and stable, with a mean $\tau_{225 \text{ GHz}}$ ranging from 0.07 to 0.09. The target observations were interleaved over a roughly 7.2 hour transit period, resulting in 190.5 minutes of on source integration time for HERS1. Observations of HERS1 were next obtained

in the SMA extended configuration (maximum baselines 220 meters) on 2016 October 16. The weather was very good, with a mean $\tau_{225 \text{ GHz}}$ of 0.04 to 0.06. The target observations were interleaved over a roughly 9.5 hour transit period, resulting in 225 minutes of on source integration time for HERS1. Last observations of HERS1 were conducted in the SMA very extended configuration (maximum baselines 509 meters) on 2017 September 30 and again on October 6 (PID: 2017A-S036; PI: Cooray). For the September 30 observation, only six antennas were available due to a cryogenics issue, which recovered in time for the October 6 observations. For the first observation the weather was very good, with a mean $\tau_{225 \text{ GHz}}$ of 0.06 (translating to 1.0 mm precipitable water vapor), and phase stability was generally very good. In the second observation, the weather was somewhat worse, with $\tau_{225 \text{ GHz}}$ rising from 0.6 to 0.085 (1 to 1.5mm pwv), with somewhat marginal phase stability. For both tracks, the target scans were interleaved over a roughly 9 hour transit period, resulting in 160 min (30 Sep) and 206 min (6 Oct) of on source integration time for HERS1. For all the observations, passband calibration was obtained using observations of 3C454.3, and gain calibration relied on periodic observations of J0224+069. The absolute flux scale was determined from observations of Uranus.

The integrated continuum visibility data for all four tracks were jointly imaged and deconvolved using the Astronomical Image Processing System (AIPS). Using natural weighting of the visibilities, the synthesized resolution is $580 \text{ mas} \times 325 \text{ mas}$ (PA 27.2 deg), and the achieved rms in the combined data map is $305 \text{ mJy beam}^{-1}$.

2.4. ALMA observation

We obtained four CO emission lines with ALMA from two programs. The CO(6-5) and CO(9-8) were obtained in project 2018.1.00922.S (PI: Riechers) on 2018 October 21 and November 30. Each execution used four spectral windows (SPW) covering the target lines. Each SPW was 2.000 GHz wide with 128 channels. Both observations were performed with ALMA 7m antennas with a maximum baseline of 48.9 m yielding the synthesis beam size $8.14'' \times 5.12''$ (PA= 76 deg) for CO(6-5) and $5.28'' \times 3.32''$ for CO(9-8) (PA= 88 deg). The band-pass and flux calibrators were J0237+2848 (CO(6-5)) and J0238+1636 (CO(9-8)). J0217+0014 was used as phase calibrator for both execution. The integration time was 18 min and 15 min reaching the root mean square (RMS) of $1.4 \text{ mJy beam}^{-1}$ over 266 MHz bandwidth (CO(6-5)) and $1.2 \text{ mJy beam}^{-1}$ over 388 MHz bandwidth (CO(9-8)) respectively. The CO(7-6) and

Table 1. Summary of emission line observations

Science goal	ν_{obs} (GHz)	t_{on} (min)	Beam size($''$)	Beam PA($^{\circ}$)	RMS (mJy beam $^{-1}$)(bandwidth)	References
CO(3-2)	97.3	62	0.45×0.32	89	0.250 (11.8MHz)	-
CO(4-3)	129.7	108	0.27×0.21	88	0.150 (23.2MHz)	1
CO(5-4)	162.2	10	10.50×5.90	-80	1.800 (221.6MHz)	-
CO(6-5)	194.6	18	8.14×5.20	76	1.400 (266.1MHz)	-
CO(7-6)	227.0	12	6.88×4.64	87	1.040 (310.6MHz)	-
CO(9-8)	291.8	15	5.28×3.32	76	1.200 (399.1MHz)	2
CI(1-0)	138.5	108	0.27×0.21	88	0.150 (23.2MHz)	1
CI(2-1)	227.8	12	6.88×4.64	87	1.040 (310.6MHz)	-
[NII] 205 μm	411.2	42	0.32×0.25	80	3.000 (15.6MHz)	3

References—1: [Geach et al. \(2018\)](#); 2: [Riechers et al. \(2021\)](#); 3: [Doherty et al. \(2020\)](#).

CO(5-4) were observed in another project 2016.2.00105S (PI: Riechers) The observation covering four frequency ranges of 211.06-214.90GHz, 226.12-229.98GHz, 147.02-150.88GHz, and 159.15-162.99GHz. Data were acquired on 2017 September 09 and 21 using ALMA 7m antennas with total on-source integration time of 11.8 and 10.3 min, respectively. Calibrators using for bandpass, flux and phase calibrations were J0006-0623, Uranus and J0217+0144. The RMS of the data reach 1.040 mJy beam $^{-1}$ over bandwidth 310.6MHz for CO(7-6) and 1.800 mJy beam $^{-1}$ over 221.6MHz bandwidth for CO(5-4). The synthesis beam were $6.88'' \times 4.64''$ at a PA of 87 deg (CO(7-6)) and $10.50'' \times 5.90''$ at a PA of 80 deg (CO(5-4)). The CI fine structure line (refer as CI(2-1) hereafter) was also detected in the same detection window of CO(7-6) at frequency $\nu_{\text{obs}} = 227.8\text{GHz}$. Table 1 lists a brief summary of ALMA observations.

2.5. Archival Observations

HERS1 was observed by extensive programs covering different bands of emission lines and continuums as mentioned above. Here we present a brief summary of the archival data of previous observation that were used in this paper.

[Geach et al. \(2018\)](#) performed an observation on 2017 December 11 and 14 (PID: 2017.1.00814.S; PI: Ivison) using the ALMA 12m array. The frequency ranges were 126.26-130.01GHz and 138.26-142.01GHz. A 1σ rms sensitivity of $150\mu\text{Jy}$ per 23MHz channel was acquired with a total 1.8 hours on-source integration. The resulting beam size is $0.27'' \times 0.21''$. The data resulted in the discovery of three emission lines, CN(4-3) at 127.6GHz, CO(4-3) at 129.8GHz, and CI(1-0) at 138.5GHz (for details see their paper). The NII(1-0) fine-structure line was also observed by this project at 441.2GHz on 26 Au-

gust 2018. A rms noise of 3 mJy beam $^{-1}$ in a 15.6MHz channel was reached after a 42min total on-source integration. The synthesis beam is $0.32'' \times 0.25''$ (Table 1).

The CO(3-2) line ($\nu_{\text{obs}} = 97.3\text{GHz}$) was detected on 2017 December 26 (PID:2017.1.01214; PI: Yun) with 12m ALMA array. The line was covered in the spectral window centered on the frequency of 97.308GHz with 480 channels. The resulting synthesized beam size was $0.45'' \times 0.32''$ and the rms was $420\mu\text{Jy beam}^{-1}$ with a bandwidth 3.9MHz (Table 1).

Apart from WFC3 F125W band, the lensing galaxy has been observed by other two HST observations, these are HST/WFC3 F110W (PID: 15242; PI: Marchetti) and HST/WFC3 160W (PID: 14653; PI: Lowenthal). Both photometry results were included in the spectral energy distribution (SED) fitting. In the SED fitting, the following observations were also adopted: *Spitzer*/IRAC 3.6 μm and 4.5 μm (PID: 14321; PI: Yan), *Herschel*/SPIRE 250 μm , 350 μm and 500 μm ([Viero et al. 2014](#)), SCUBA 850 μm , AzTEC 1.1mm ([Geach et al. 2015](#)), IRAM 1.3 mm, and ACT 2.026 mm ([Su et al. 2017](#)).

3. LENS MODEL

3.1. HERS1

HERS1 is a gravitationally lensed galaxy magnified by two foreground galaxies (a primary galaxy G1 and a satellite G2 located at the northwest of G1 shown in Figure 1) at the same redshift $z = 0.202$. In order to derive its intrinsic properties, we first built a lens model of this system.

We used the publicly available code LENSTOOL¹ to construct the best-fit model. The best-fit parameters were found by performing a Bayesian Markov Chain Monte Carlo (MCMC) sampling. The lensing system is mainly made of two parts as shown in Figure 1. We used HST/WFC3 F125w high-resolution image to constrain the lens model parameters. We first fitted the light profile of the lensing galaxies (G1 and G2) by a Sérsic function using GALFIT (Peng et al. 2010). We then subtracted the modeled foreground galaxies to obtain the lensed image. We also examined a multi-component function (E. Borsato, private communication) to model lensing galaxies, but found no significant difference in the resultant lensed image. Therefore, we kept the simpler model defined by a single Sérsic function. The lensed components were then identified using PHOTUTILS² package (Bradley et al. 2020) and broken into four ellipses. The elliptical size and fluxes of these ellipses were then measured as input information of LENSTOOL. We chose a singular isothermal ellipsoid profile for the primary galaxy G1 and a singular isothermal sphere profile for G2. We fixed the positions of the galaxies, so the model was parametrized by the ellipticity e , the position angle θ and the velocity dispersion σ_1 for G1 and velocity dispersion σ_2 for G2. The redshift of foreground galaxies and background galaxy was fixed at $z = 0.202$ and $z = 2.553$, respectively. The optimization output provided the best-fit results. Table 2 gives the best-fit parameters of the lensing galaxies. The reconstructed images obtained from the best-fit model are shown in Figure 2. From this model, we obtain the luminosity-weighted magnification factor is $\mu_{\text{star}} = 13.6 \pm 0.4$. The best-fit model established above was also used to reconstruct images of the aforementioned high resolution emission lines and SMA dust continuum as shown in Figure 3. The dust map provides a magnification factor $\mu_{\text{dust}} = 12.8 \pm 0.3$. The source plane images are reconstructed using the CleanLens algorithm within LENSTOOL, the results are also illustrated in 2 and Figure 3.

3.2. Second Lensed Source

In the high-resolution HST data, an additional clump is detected as shown in Figure 4. Our model does not have a predicted counter-image in that position. We traced this part to source plane using the best-fit model above, the corresponding source located in the north-east of the main source as shown in Figure 4 which suggests it is an extra individual component. S2 is also de-

tected in ALMA [NII] 205 μm (data from Geach et al. 2018) and described in (Doherty et al. 2020). While this study failed to identify the detection with a second source, we confirm the presence of S2 at the same redshift as S1 through a combination of HST/WFC3 and [NII] observations. The line profiles of S1 and S2 are compared in Figure 5. The extra component has a narrower line width which also implies that it comes from a different region. As the detections are limited to rest-frame optical in HST/WFC3 and [NII] 205 μm with ALMA, further observations are needed to fully understand this component.

Table 2. Lens modelling results and Surface brightness model for lensing galaxies

Lensing model			
Object	Quality	Value	Unit
G1	e	0.34 ± 0.06	...
...	θ	-8 ± 2	deg
...	σ_1	318 ± 3	km s^{-1}
...	RA	02:09:41.27	h:m:s
...	Dec	+00:15:58.53	d:m:s
...	z	0.202	...
G2	σ_2	66 ± 10	km s^{-1}
...	RA	02:09:41.24	h:m:s
...	Dec	+00:16:00.84	d:m:s
...	z	0.202	...
Surface brightness model			
G1	R_e	18	pixel
...	n	3.2	...
...	b/a	0.93	...
...	PA	119	deg
G2	R_e	3	pixel
...	n	1.3	...
...	b/a	0.95	...
...	PA	118	deg

4. PHYSICAL PROPERTIES

4.1. CO line properties

CO SLED is an effective tool that can be used to reveal the bulk physical properties of a galaxy. HERS1 has multiple CO line detections up to $J_{\text{up}} = 11$. We first calculated the observed CO SLED combining the data in this paper and the results from the literature (Geach et al. 2018; Harrington et al. 2021). Figure 6 shows the line variations normalized by CO(1-0). Other well-studied systems are also shown for comparison (Fixsen et al. 1999; Papadopoulos et al. 2012; Bothwell et al. 2013; Carilli & Walter 2013; Riechers et al.

¹<http://projets.lam.fr/projects/lenstool/wiki>

²<https://photutils.readthedocs.io/en/stable/>

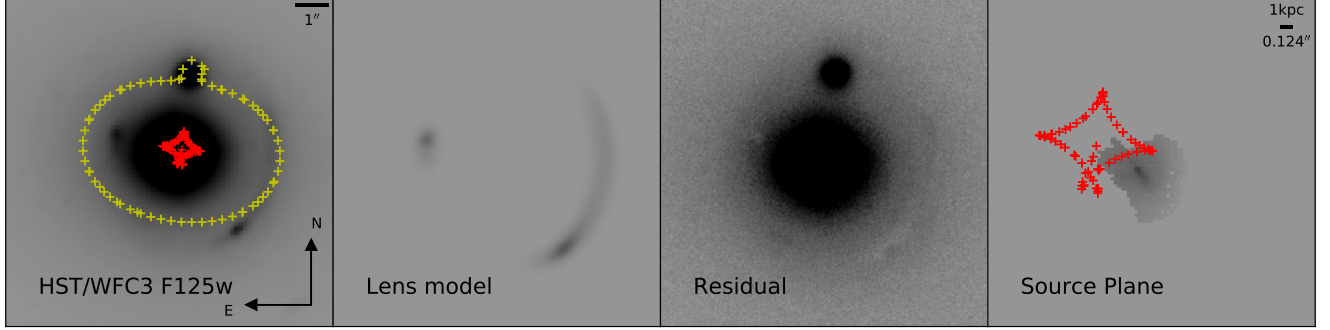


Figure 2. Lens modelling results of HERS1. First column: HST/WFC3 F125W band image of HERS1 with two foreground galaxies and a partial Einstein Ring observed. The yellow and red curves are the critical and caustic lines derived from the best-fit model. Second column: the reconstructed lens plane image of the best-fit model results. Third column: the residual map after subtracting the model from the original image. Last column: the source plane reconstruction along with caustic line.

2013). Overall, the CO flux increases with J_{up} and peaks at $J_{\text{up}} = 6$, then declines toward higher rotation numbers. The excitation is higher than the average of SMGs but not as high as the extremely excited galaxies such as APM08279 and HFLS-3. The ladder shape is also similar to some local ULIRGs and starburst galaxies (Rosenberg et al. 2015; Mashian et al. 2015).

In order to further study the intrinsic properties of the source, we applied the magnification correction to these line intensities. Due to lack of data of some lines, we only calculated the de-lensed fluxes of line $J_{\text{up}} = 3, 4, 5, 6, 7, 9$. For line CO(3-2) and CO(4-3), we first rebinned the data to width of 36 km s^{-1} and calculated the magnification factor on each channel map based on the best-fit lens model and high resolution lensed image. The results are shown in Figure 7 (CI and [NII] line are presented as well using the same method). For lines with $J_{\text{up}} \geq 5$, we adopted the magnification factor of CO(4-3) velocity channels due to lack of high-resolution images. It is suggested that differential lensing may cause a bias on the CO SLED calculation. Serjeant (2012) shows the 1σ dispersion of CO(6-5) can reach to 20 percent of the mean value for $500 \mu\text{m}$ -selected sources with $\mu > 10$. Frequency-dependent lens models are required to verify our assumption but this is beyond the scope of this paper. Though differential lensing distort the CO SLED, the mid-J lines may have similar distortion. The linewidths of our CO lines are close to each other which implies they arise from similar emission regions and this is consistent with the assumption. So we consider using the magnification factor of CO(4-3) as the factor of higher J_{up} lines is a moderate assumption. Figure 8 shows the observed and de-lensed line profiles.

The observed line fluxes present a double-horn profile, this feature becomes more obvious after correcting magnification on each velocity channel. We also separated

the line profile into two individual components, a ‘blue’ part and a ‘red’ part based on their velocity. A double-Gaussian model was used to fit each de-lensed line by fixing the peak separation ($\Delta v = 419 \text{ km s}^{-1}$) and full-widths-at-half-maximum ($\text{FWHM}_b = 221 \text{ km s}^{-1}$, $\text{FWHM}_r = 209 \text{ km s}^{-1}$). The model lines were also illustrated in Figure 7 and Figure 8. Velocity-integrated flux densities were then measured from the Gaussian functions. Results are reported in Table 3. The intrinsic SLED of the total source as well as the individual components were also shown in Figure 9. As we can see, the magnification factors vary with the velocity. The blue components have higher magnification than the red components, so the de-lensed flux profiles show more symmetry forms comparing to the observed spectrums.

To further investigate the molecular gas, we apply the LVG code on CO SLED. We adopt the code RADEX (van der Tak, F. F. S. et al. 2007) to fit our CO fluxes. RADEX is non-LTE analysis code to compute the atomic and molecular line intensities with an escape probability of $\beta = (1 - e^{-\tau})/\tau$. CO collision files are taken from Leiden Atomic and Molecular Database (LAMDA)(Schöier, F. L. et al. 2005).

The input parameters of RADEX includes: the molecular gas kinetic temperature T_k , the volume density of molecular hydrogen n_{H_2} , the column density of CO, N_{CO} and the solid angle of the source. The velocity gradient is fixed to 1 km s^{-1} , so the CO column density N_{CO} also equals to the column density per unit velocity gradient N_{CO}/dv . We only concern about the first three parameters, T_k , n_{H_2} , N_{CO}/dv , because the resulting CO SLED shape is not depend on the solid angle. Instead of using RADEX grids which produce a grid of CO emission fluxes given a range of parameters, we adopted a Bayesian method and performed an MCMC calculation to fit RADEX results with the

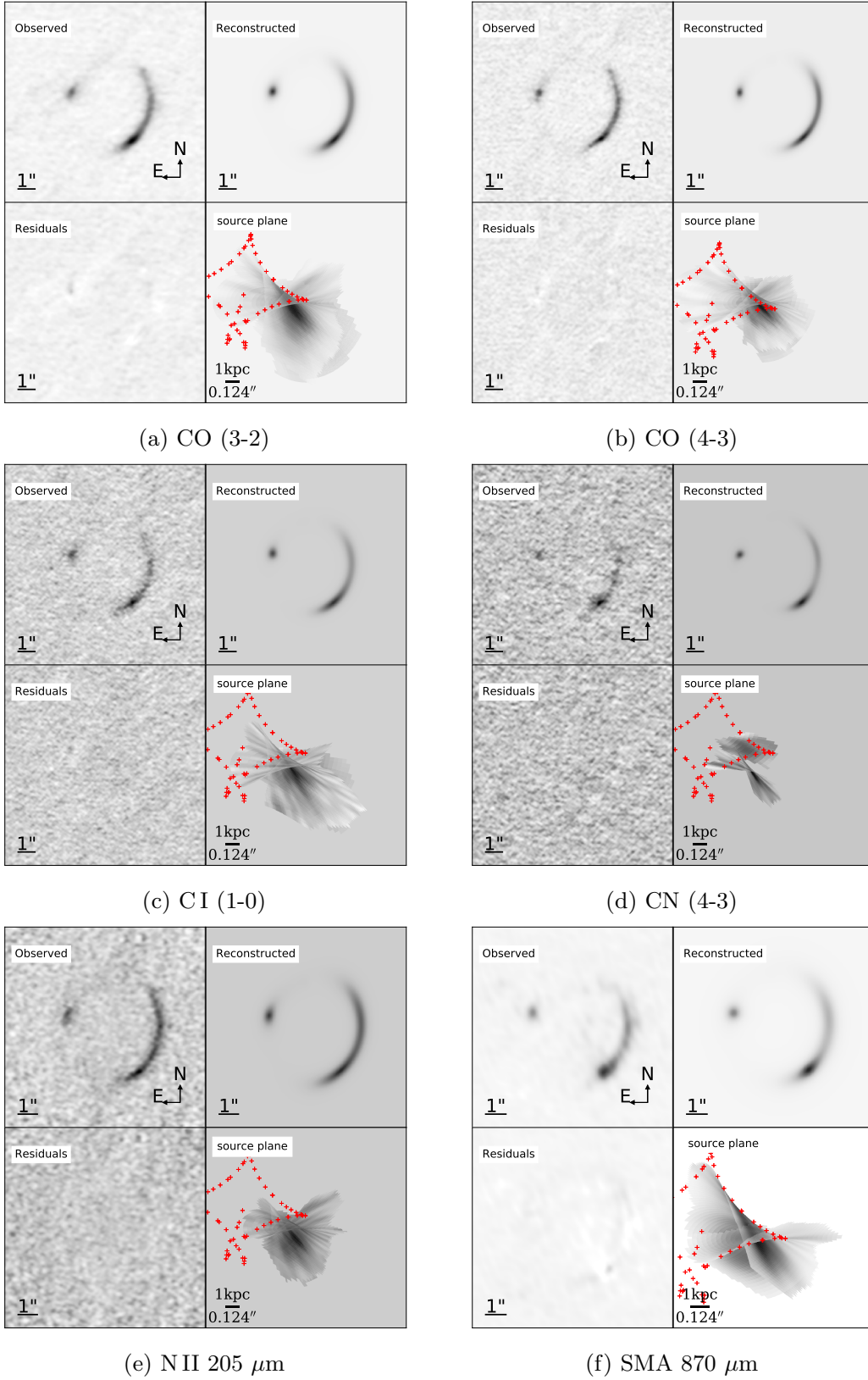


Figure 3. Observation of emission lines from ALMA and SMA 870 μm along with modelling results using the best-fit model derived from high-resolution HST image. Label (a)-(f) list the line species. The channel-dependent source plane reconstructions are available in the online version of the paper.

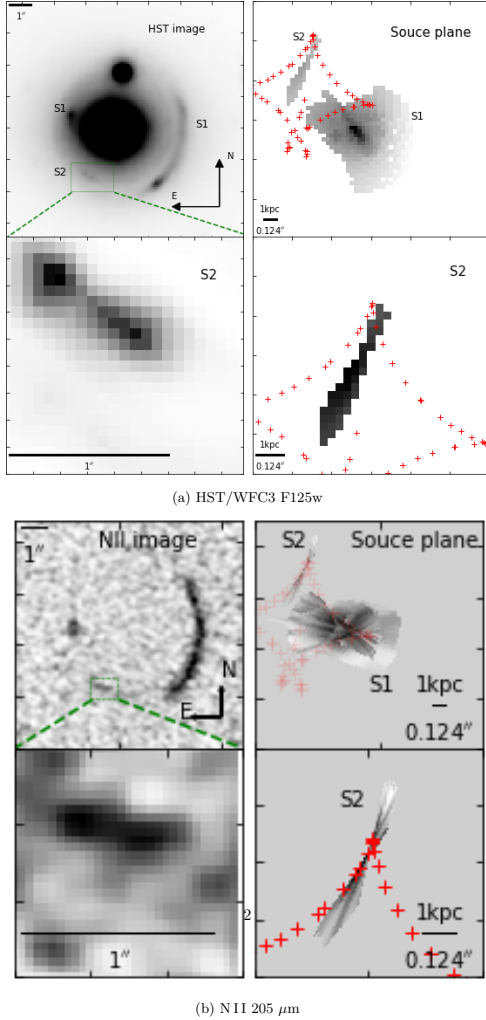


Figure 4. Panel (a) left: HST/WFC3 F125w image. Upper panel shows the entire image of the lensed arcs. The green dashed box displays the position of the additional clump. A zoomed in image of this part is shown in the lower panel. Right: source plane reconstructions with caustic line overplotted in red using the best-fit model. Upper panel shows the reconstruction of all lensed arcs with S1 corresponds to HERS1 and S2 corresponds to the additional clump. Lower panel shows a zoomed in image of S2. Panel (b): NII 205 μm images in the same order as panel a.

observed fluxes. This allows a faster convergence and a better sampling in the parameter space (Yang et al. 2017). The code RADEX.EMCEE was used for the calculation³. This package combines PYRADEX⁴, a PYTHON version of RADEX converted by Ginsburg, and EMCEE⁵ to achieve the fitting.

³https://github.com/yangcht/radex_emcee

⁴<https://github.com/keflavich/pyradex>

⁵<https://github.com/dfm/emcee>

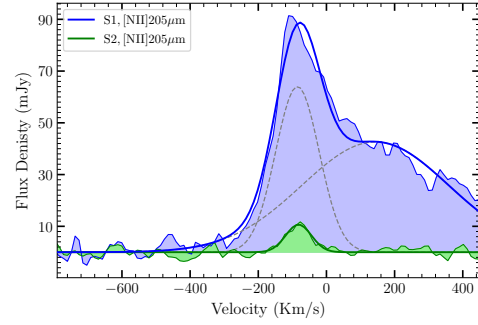


Figure 5. Observed [N II] 205 μm spectral profile of HERS1 and the additional clump for comparison. The blue component shows the line profile of HERS1, solid blue line demonstrate the double-Gaussian fit result with the individual components overlaid in grey dash lines. The green component corresponds to the profile of the additional clump. A single Gaussian function was used as shown in solid green line.

Previous studies show that the CO emissions are likely dominated by two components (e.g. Daddi et al. 2015; Yang et al. 2017; Cañameras et al. 2018) and a single-component model is inadequate for fitting our SLED. So we adopted a two-component model including a warmer high-excitation component and a cooler low-excitation component in our fitting as the one-component model poorly fitted the CO SLED. That model allows two sets of parameters for different physical conditions of the two components. We applied the flat log-prior for n_{H_2} , N_{CO}/dv (e.g. Spilker et al. 2014). The ranges of the parameters are taken as $n_{\text{H}_2} = 10^2 - 10^7$, $N_{\text{CO}} = 10^{15.5} - 10^{19.5}$ for both two components. An extra limit of dv/dr with a range of $0.1 - 1000 \text{ km s}^{-1}$ is adopted (e.g. Tunnard & Greve 2016), this provided a limit of the ratio between N_{CO}/dv and n_{H_2} . For the kinetic temperature, two different prior ranges were chosen. The warmer component also have a flat log-prior with a range $T_k = T_{\text{CMB}} - 10^3 \text{ K}$, where T_{CMB} is the CMB temperature at the redshift of the source. For the cooler part, we set an additional limit that the temperature was close to the temperature of cold dust. As discussed by Goldsmith (2001), the temperature of gas and dust couple well at high density $N_{\text{H}_2} \geq 10^{4.5} \text{ cm}^{-3}$, but this relation is not satisfied when $n_{\text{H}_2} \leq 10^{3.5} \text{ cm}^{-3}$. So we took a normal distribution of the cooler component which gave a reasonable guess in the range $T_{\text{CMB}} - 90 \text{ K}$. Besides, the size of the cooler component was set to be larger than the warmer component inspired by observations of the size of different CO line emission regions (e.g., Ivison et al. 2011b).

Figure 10 and Figure 11 show the best-fitting two-component results. The low-excitation gas component

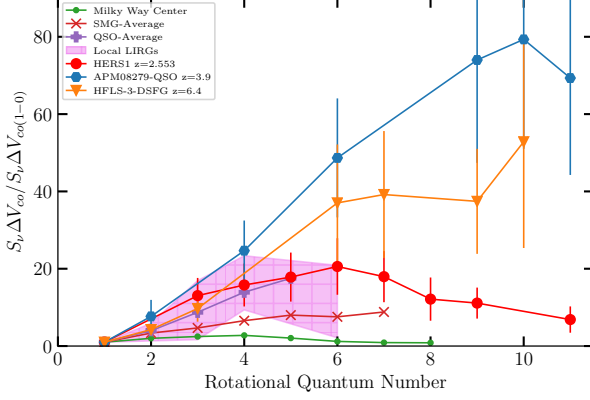


Figure 6. Observed CO SLEDs normalized by CO(1-0) flux density with other well-studied systems for comparison.

Table 3. Integrated line flux densities of two kinematic components and the overall lines in the source.

line(CO)	I_b (Jy km s ⁻¹)	I_r (Jy km s ⁻¹)	I (Jy km s ⁻¹)	Refs
(1-0)	-	-	0.17 ± 0.06	1
(3-2)	1.21 ± 0.09	1.22 ± 0.08	2.42 ± 0.12	-
(4-3)	1.29 ± 0.10	1.30 ± 0.09	2.59 ± 0.13	2
(5-4)	1.38 ± 0.07	1.41 ± 0.07	2.79 ± 0.10	-
(6-5)	1.34 ± 0.07	1.89 ± 0.07	3.23 ± 0.10	-
(7-6)	1.28 ± 0.08	1.51 ± 0.08	2.79 ± 0.12	-
(8-7)	-	-	2.08 ± 0.21	1
(9-8)	0.88 ± 0.06	0.95 ± 0.06	1.84 ± 0.09	3
(11-10)	-	-	1.17 ± 0.18	1

References—1: [Harrington et al. \(2021\)](#); 2: [Geach et al. \(2018\)](#); 3: [Riechers et al. \(2021\)](#)

peaks at $J_{\text{up}} = 2-3$ while the high-excitation gas peaks at $J_{\text{up}} = 6-7$ with a higher temperature and CO density as shown in the global SLED model. The two individual kinematic components were then fitted in the same way. The two spectral components show similar excitation compositions to the global profile. Most properties of the two spectral components are thus similar to the overall gas while the low-excitation component of the blue part shows a higher kinetic temperature and the red part exhibits a denser CO density. The results are also similar to other studies of high-redshift SMGs(e.g. [Spilker et al. \(2014\)](#); [Yang et al. \(2017\)](#)).

4.2. FIR spectral energy distribution and inferred parameters

We fit the SED using the publicly available SED-fitting package MAGPHYS ([Da Cunha et al. 2008](#)). MAGPHYS provides a library of model templates based on a largely empirical but physically motivated model. The stellar light is computed using the [Bruzual & Char-](#)

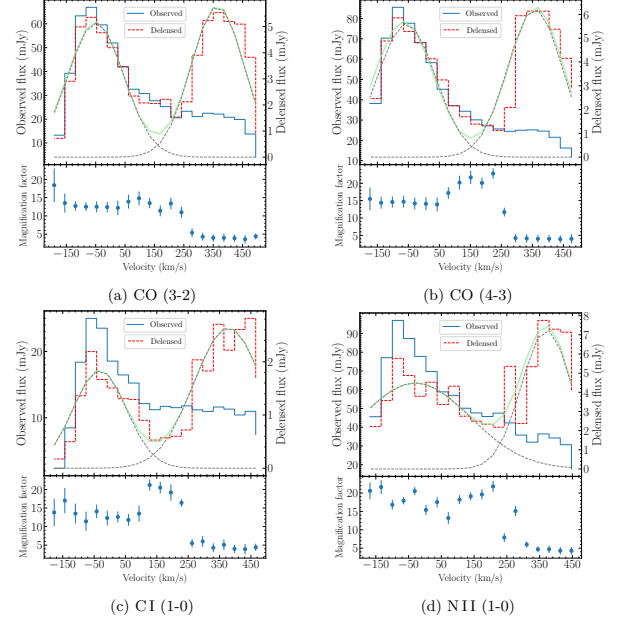


Figure 7. (a)-(d): Spectral lines from observations with high-resolution lensed images. In each subpanel, upper component shows the de-lensed (dashed red line) and observed (solid blue line) spectra. The de-lensed line was fitted with a double-Gaussian model by fixing the FWHM of each component and the width between two peaks. The best-fit result is shown as solid green curve while the individual components are overlaid in dashed grey. Lower panels show the magnification factor for each velocity channel.

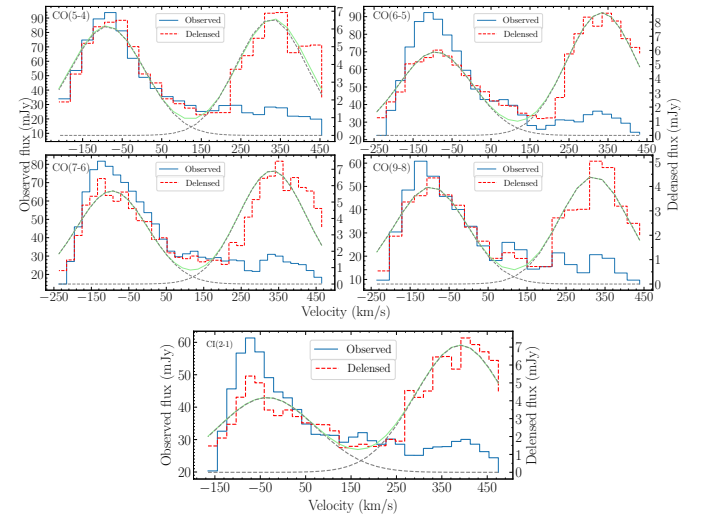


Figure 8. Same as Figure 7, but show the high J_{up} CO and CI lines. The magnification factor is taken from CO(4-3) for CO lines and CI (1-0) for CI (2-1) line.

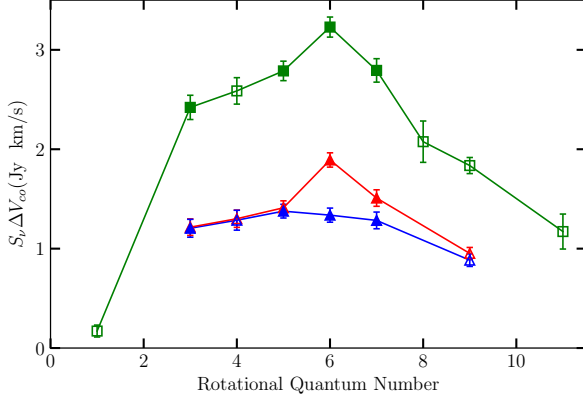


Figure 9. Velocity integrated line fluxes corrected for magnification. Green symbols represent the total flux densities. Data points plotted with open squares were described in Geach et al. (2018); Harrington et al. (2021); Riechers et al. (2021). Red and blue symbols show the flux densities of red and blue kinematic components respectively.

lot (2003) synthesis code and the attenuation is described by a two-component model of (Charlot & Fall 2000) which gives the infrared luminosity absorbed and re-radiated by the dust (Da Cunha et al. 2008). Depending on the redshift of the background, high- z extension version (Cunha et al. 2015) which extend the SED parameter priors to the high redshift was used.

Multiband fluxes were required by MAGPHYS. We used the data includes HST/WFC3 F110W, F125W, F160W data, Keck H and K_s data, *Spitzer*/IRAC 3.6 μm , and 4.5 μm data, the observation from *Herschel*/SPIRE 250 μm , 350 μm , 500 μm and data from SCUBA 850 μm , SMA 870 μm , AzTEC 1.1 mm, IRAM 1.3 mm, and ACT22 2.026 mm. These results are listed in Table 4. We corrected the data by magnification and fixed the redshift as the input of MAGPHYS. The best-fit SED result is shown in Figure 12 and Table 5. The differential lensing effect was also considered to be negligible because all of the current continuum models have similar magnify factors. From the best-fit SED model, we can derive the total intrinsic infrared luminosity of HERS1, $L_{\text{IR}} = (1.0 \pm 0.3) \times 10^{13} L_{\odot}$, which makes it one of Hyperluminous galaxies at high-redshift. The corresponding star formation rate is $1023 \pm 264 M_{\odot} \text{yr}^{-1}$ assuming a Chabrier initial mass function (Chabrier 2003) and a convert formula $\text{SFR} = 1 \times 10^{-10} L_{\text{IR}}$. HERS1 also possesses a large value of stellar mass which is in agreement with simulations (Davé et al. 2010) and model requirements of sub-millimeter bright galaxies (Hayward et al. 2011). The stellar mass and SFR relation is shown in the top panel of Figure 13. It is suggested that there is a tight correlation (called ‘main sequence’) between the SFR and stellar mass for the majority of star-forming

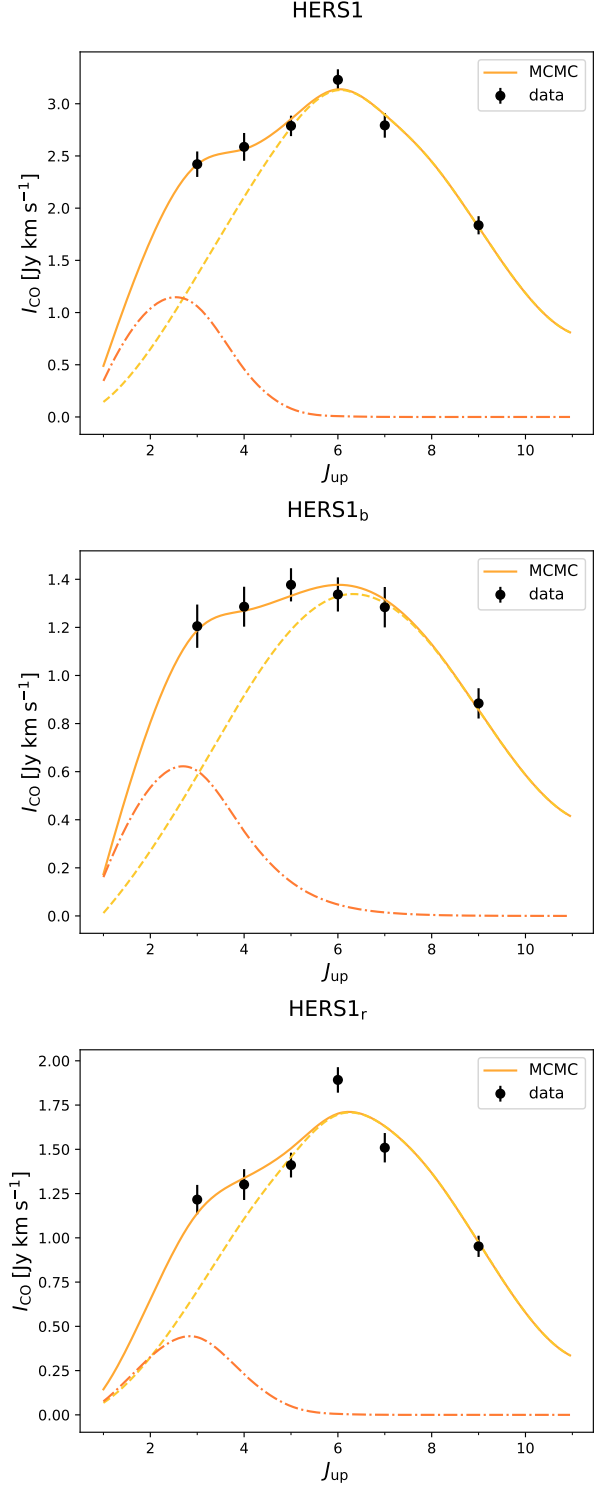


Figure 10. Top: de-lensed CO SLED of HERS1 and the best-fit LVG model using two excitation components (solid orange line). The dot-dashed red line and dashed orange line represent the lower and higher excitation components respectively. Middle: same as top panel but shows the result of blue kinematic component. Bottom: same as top panel but shows the result of red kinematic component.

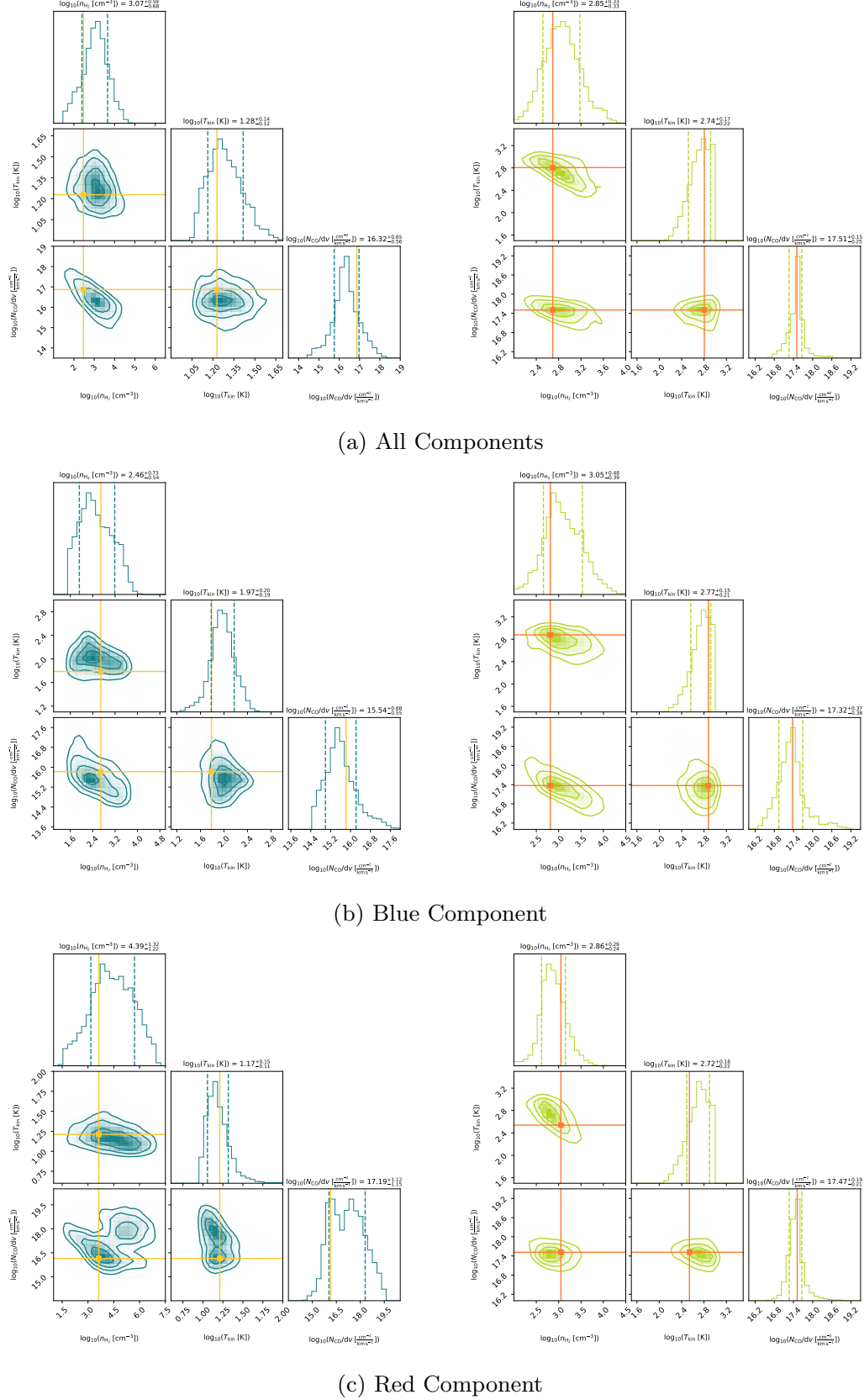


Figure 11. Posterior probability distribution of n_{H_2} , T_{kin} and N_{CO}/dv derived from the MCMC sampling of the two components model. Solid lines show the maximum posterior probability of each parameter while the dashed lines show the $\pm 1\sigma$ range. The results are also listed on each histogram. The left panel corresponds to the lower excitation component while the right panel corresponds to the higher component. From top to bottom are the results of the total SLED, the blue and red kinematic components, same order as Figure 10.

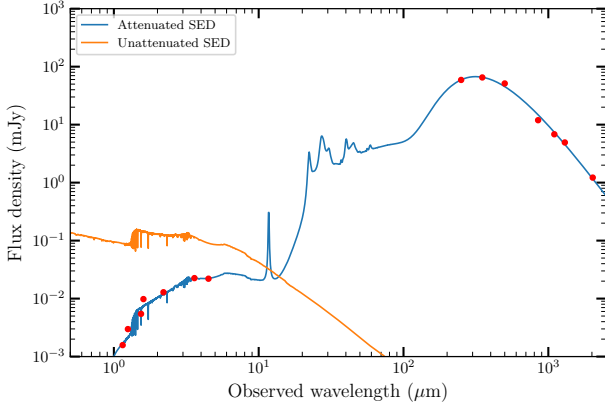


Figure 12. Best-fit SED of HERS1 using the de-magnified flux densities in MAGPHYS. Blue line shows the attenuated SED while orange line shows the unattenuated SED. Red points are the de-magnified photometric results.

galaxies both in the local and high redshift. Figure 13 presents the $z=2.6$ ‘main sequence’ of Speagle et al. (2014) with a scatter of 0.2 dex. As we can see, HERS1 has a higher SFR than the ‘main sequence’ value at the corresponding stellar mass. The huge molecular gas reservoirs are available to meet the intense star formation activities. For the dust temperature, the best-fit result is $T_d = 35.1^{+1.9}_{-1.4}$ K. The dust temperature is correlated with the infrared luminosity for both local infrared luminous SMGs and high-redshift far-infrared or sub-millimeter selected galaxies as shown by many works (Chapman et al. 2005; Hwang et al. 2010; Magdis et al. 2010; Elbaz et al. 2011; Casey et al. 2012; Magnelli et al. 2012, 2014; Symeonidis et al. 2013; Béthermin et al. 2015). It is a useful way to study different galaxy populations using the $L_{\text{IR}} - T_d$ relation. The dust temperature of galaxies at high-redshift are likely bias to a cooler value compare with local galaxies with the same luminosities. Hwang et al. (2010) found a modest evolution of $L_{\text{IR}} - T_d$ relation as a function of redshift using HERSCHEL-selected samples out to $z \sim 2-3$. They concluded that SMGs are on average 2–5 K cooler than the local counterpart from their observation. A larger scatter of the relation at high-redshift is also possible found by Magnelli et al. (2012) while this can be reconciled with the results of Hwang et al. (2010) by considering selection effects. Figure 14 shows the dust temperature and infrared luminosities of HERS1 with submillimeter and HERSCHEL-selected SMGs at $z \sim 2-3$. Comparing with these galaxies, HERS1 has a colder temperature similar with other lensed candidate samples of Nayyeri et al. (2016).

4.3. Molecular Gas and CI

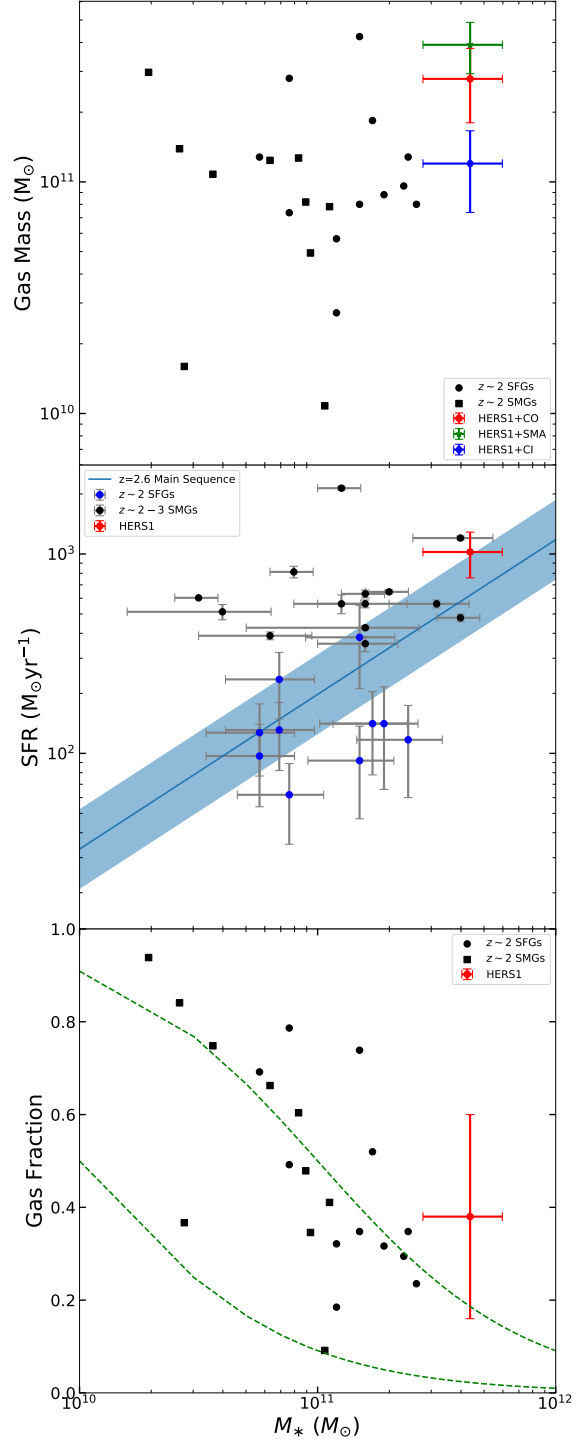


Figure 13. Top: molecular gas mass calculated from CO(1-0) (red), CI lines (blue) and SMA 870 μm (green) along with SFGs and SMGs at similar redshift (Genzel et al. 2010; Bothwell et al. 2013). Middle: stellar mass vs. star formation rate of HERS1. The blue line and shadow blue area show the $z = 2.6$ trend and a 0.2 dex scatter suggested by Speagle et al. (2014). SFGs at $z \sim 2$ and SMGs at $z \sim 2-3$ (Genzel et al. 2010; Ivison et al. 2011a; Magnelli et al. 2012) are presented for comparison. Bottom: similar with top panel but shows molecular gas fraction. The fraction of HERS1 takes the average value of three HERS1 data. The green dash lines represent a constant stellar mass of $10^{10} M_\odot$ and $10^{11} M_\odot$, respectively.

Table 4. Photometry of HERS1

Instrument	Flux Density
HST/WFC3 F110W	$15.1 \pm 0.8 \mu\text{Jy}$
HST/WFC3 F125W	$23.5 \pm 1.4 \mu\text{Jy}$
HST/WFC3 F160W	$61.4 \pm 2.2 \mu\text{Jy}$
KECK H	$137.3 \pm 1.9 \mu\text{Jy}$
KECK K_s	$180.1 \pm 2.3 \mu\text{Jy}$
<i>Spitzer</i> /IRAC 3.6 μm	$315.8 \pm 12.0 \mu\text{Jy}$
<i>Spitzer</i> /IRAC 4.5 μm	$308.4 \pm 11.9 \mu\text{Jy}$
<i>Herschel</i> /SPIRE 250 μm	$826 \pm 7 \text{ mJy}$
<i>Herschel</i> /SPIRE 350 μm	$912 \pm 7 \text{ mJy}$
<i>Herschel</i> /SPIRE 500 μm	$718 \pm 8 \text{ mJy}$
SCUBA 850 μm	$167 \pm 4 \text{ mJy}$
SMA 870 μm	$160 \pm 3 \text{ mJy}$
AZTEC 1.1 mm	$95.5 \pm 2.4 \text{ mJy}$
IRAM 1.3 mm	$69 \pm 2.7 \text{ mJy}$
ACT22 2.026 mm	$17.1 \pm 1.6 \text{ mJy}$

NOTE—The observed flux densities were de-magnified in the SED fitting. The HST, Keck, and *Spitzer* data were demagnified by 13.6 ± 0.4 and other data were de-magnified by 12.8 ± 0.3 .

Table 5. Derived properties of HERS1 from SED fitting

Quantity	Value	Unit
M_*	$4.3^{+2.2}_{-1.0} \times 10^{11}$	M_\odot
M_d	$2.6 \pm 0.3 \times 10^9$	M_\odot
T_d	$35.1^{+1.9}_{-1.4}$	K
L_{IR}	$1.0 \pm 0.3 \times 10^{13}$	L_\odot
SFR	1023 ± 264	$M_\odot \text{yr}^{-1}$
z	2.553	...

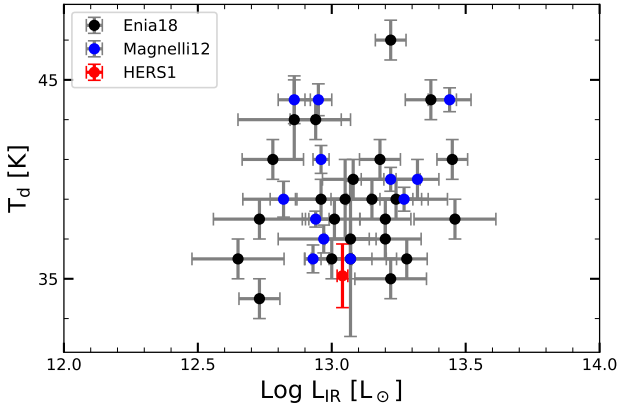


Figure 14. Dust temperature vs. FIR luminosity. The $z \sim 2 - 3$ SMGs (Magnelli et al. 2012; Enia et al. 2018) are plotted for comparison.

The intrinsic luminosity $L'_{\text{CO}(1-0)}$ of CO(1-0) is $(5.12 \pm 1.81) \times 10^{10} \text{ K km s}^{-1} \text{ pc}^2$ using the GBT data observed by Harrington et al. (2021) as mentioned above. The molecular gas is $(2.79 \pm 0.99) \times 10^{11} M_\odot$ adopting a conversion factor $\alpha_{\text{CO}} = 4.0 M_\odot (\text{K km s}^{-1} \text{ pc}^2)^{-1}$ and taking into the a factor 1.36 for helium. The conversion factor α_{CO} is one of the main uncertainty sources of the molecular gas mass determined from CO line luminosity. Different values were taken for various types of galaxies. Previous studies chose $\alpha_{\text{CO}}=0.8$ which was commonly used for star-formation galaxies when converting CO(1-0) luminosity into gas mass. Combining with dust mass derived in the SED fitting, the lower α_{CO} value results a very low gas/dust ratio (~ 20) which makes it become an extreme case. So we take a higher value which is canonical for local galaxies in this paper. We also calculated the gas mass from SMA data using the empirical calibration of Scoville et al. (2014). The result is $(4.49 \pm 1.12) \times 10^{11} M_\odot$ which also suggests a higher conversion factor value. Having the gas mass and star-formation rate, we can derive the gas depletion timescale $t_{\text{dep}} \equiv M_{\text{gas}}/\text{SFR}$. HERS1 has a gas depletion of ~ 257 Myr, this is much smaller than the star-forming galaxies ~ 1 Gyr (e.g. Kennicutt 1998; Genzel et al. 2010; Saintonge et al. 2011; Decarli et al. 2016a,b) and a ‘main sequence’ ~ 0.7 Gyr or even shorter (Tacconi et al. 2013; Sargent et al. 2014; Saintonge et al. 2013). The gas fraction f_{gas} can be calculated as $M_{\text{gas}}/(M_* + M_{\text{gas}})$. HERS1 has a low gas fraction with $f_{\text{gas}} = 0.38 \pm 0.22$ as shown in the top panel of Figure 13, the low gas fraction and high stellar mass indicate HERS1 has formed most of its stars.

The observation of CO(7-6) also had a detection of CI(2-1) line at 227.79 GHz ‘for free’. We traced CI line into source plane using the same method as high-J CO lines. The result is shown in Figure 8 as well. It is suggested that CI lines arise from the same region as low-J CO transitions and can be used to derive the gas properties without other information. The intrinsic luminosity of CI(2-1) from our observation is $L'_{\text{CI}(2-1)} = (1.60 \pm 0.22) \times 10^{10} \text{ K km s}^{-1} \text{ pc}^2$. Combining the CI(1-0) observation mentioned above (the intrinsic luminosity is $L'_{\text{CI}(1-0)} = (1.65 \pm 0.20) \times 10^{10} \text{ K km s}^{-1} \text{ pc}^2$), we can derive the carbon excitation temperature $T_{\text{ex}} = 50\text{K}$ from their ratio using the formula $T_{\text{ex}} = 38.8\text{K}/\ln[2.11/R_{\text{CI}}]$ with R_{CI} is the ratio between CI(2-1) and CI(1-0) luminosity. The carbon mass was estimated then following Weiß et al. (2003), $M_{\text{CI}} = (2.16 \pm 0.26) \times 10^7 M_\odot$. The atomic carbon can also be an effective tracer to measure the gas mass. Jiao et al. (2017) found a tight correlation of luminosities between CO(1-0) and CI lines in the local (U)LIRGs. This

correlation was also valid in the high-redshift SMG samples of Yang et al. (2017). Assuming the atom carbon abundance $X[\text{CI}]/X[\text{H}_2] = M(\text{CI})/(6M(\text{H}_2)) = 3 \times 10^{-5}$, the gas mass is $(1.20 \pm 0.46) \times 10^{11} M_\odot$. This value is slightly lower than the mass derived from CO and SMA data above. However, Jiao et al. (2021) report a lower value for $X[\text{CI}]/X[\text{H}_2]$, resulting in a more consistent gas mass estimation.

5. SUMMARY

We present a detailed study of an extremely luminous sub-millimeter galaxy at $z = 2.553$, gravitationally lensed by two foreground galaxies at $z = 0.202$. The lensed galaxy, dubbed HERS1, features partial Einstein-ring with a radius $\sim 3''$ observed in high-resolution maps of HST/WFC3, SMA and ALMA. Based on the reconstructed lens model, we find magnification factors $\mu_{\text{star}} = 13.6 \pm 0.4$ and $\mu_{\text{dust}} = 12.8 \pm 0.3$ for stellar and dust emissions of HERS1, respectively. We perform SED fitting on multi-band photometry of HERS1, corrected for magnification, to measure its physical properties including stellar mass $M_* = 4.3 \times 10^{11} M_\odot$, star formation rate $\text{SFR} = 1023 M_\odot \text{yr}^{-1}$, and dust temperature $T_d = 35\text{K}$.

We analyze the physical conditions of the molecular gas through CO SLED modeling and find that its low-excitation component has a gas density $n_{\text{H}_2} = 10^{3.1} \text{cm}^{-3}$, and kinetic temperature $T_k = 19\text{K}$, while high-excitation component has $n_{\text{H}_2} = 10^{2.8} \text{cm}^{-3}$, and $T_k = 549\text{K}$. We also find that HERS1 shows higher excitation compared to an average SMG. We further derive total molecular gas of HERS1 using three distinct tracers including CO(1-0), CI lines and SMA 870 μm . We measure a gas fraction $f_{\text{gas}} = 0.38$ with a depletion time $t_{\text{dep}} \sim 250 \text{Myr}$. The short gas depletion time, compared to 1 Gyr for typical SFGs at $z \sim 2$, suggests that HERS1 will become quiescent shortly in the lack of cool gas replenishment. The location of HERS1 on $\text{SFR}-M_*$ relation shows that it is located on the massive end of the main sequence of star formation. It reveals that HERS1 has formed the bulk of its stellar mass by $z \sim 2.5$, and is about to enter a quiescent phase through the halt of cool gas replenishment possibly caused by feedback or environmental processes.

Moreover, we report the detection of another lensing arc feature in deep HST/WFC3 images. The feature is also detected in [N II] 205 μm , implying that it is at the same redshift as HERS1. We compare [N II] 205 μm line

profile of this feature with that of HERS1 and find that the extra lensing feature has a narrower line width. We thus conclude that this extra feature is originated from a different region. Due to the lack of high signal-to-noise multi-band detections, further deep observations are needed to fully understand the physical properties of this extra lensing component.

ACKNOWLEDGEMENT

Financial support for this work was provided by NSF through AST-1313319 for HN and AC. AC, HN and NC acknowledge support from NASA ADAP 80NSSC20K04337 for archival data analysis of bright *Herschel* sources. UCI group also acknowledges NASA support for *Herschel*/SPIRE GTO and Open-Time Programs. BL is supported by the China Scholarship Council grant (CSC No. 201906040079). Z-HZ is supported by the National Natural Science Foundation of China under Grants Nos. 11633001, 11920101003 and 12021003, the Strategic Priority Research Program of the Chinese Academy of Sciences, Grant No. XDB23000000 and the Interdisciplinary Research Funds of Beijing Normal University. EB and EMC are supported by MIUR grant PRIN 2017 20173ML3WW-001 and Padua University grants DOR1885254/18, DOR1935272/19, and DOR2013080/20. This paper makes use of the following ALMA data: ADS/JAO.ALMA#2016.2.00105.S and ADS/JAO.ALMA#2018.1.00922.S. ALMA is a partnership of ESO (representing its member states), NSF (USA) and NINS (Japan), together with NRC (Canada), MOST and ASIAA (Taiwan), and KASI (Republic of Korea), in cooperation with the Republic of Chile. The Joint ALMA Observatory is operated by ESO, AUI/NRAO and NAOJ. The National Radio Astronomy Observatory is a facility of the National Science Foundation operated under cooperative agreement by Associated Universities, Inc. The authors wish to extend special thanks to those of Hawaiian ancestry on whose sacred mountain we are privileged to be guests. Without their generous hospitality, most of the observations presented herein would not have been possible. The Submillimeter Array is a joint project between the Smithsonian Astrophysical Observatory and the Academia Sinica Institute of Astronomy and Astrophysics and is funded by the Smithsonian Institution and the Academia Sinica.

REFERENCES

- B  thermin, M., Daddi, E., Magdis, G., et al. 2015, *A&A*, 573, A113
- Bigiel, F., Leroy, A., Walter, F., et al. 2008, *AJ*, 136, 2846

- Bothwell, M. S., Smail, I., Chapman, S. C., et al. 2013, *Monthly Notices of the Royal Astronomical Society*, 429, 3047
- Bradley, L., Sipőcz, B., Robitaille, T., et al. 2020, *astropy/photutils*: 1.0.0, doi:10.5281/zenodo.4044744
- Bruzual, G., & Charlot, S. 2003, *Monthly Notices of the Royal Astronomical Society*, 344, 1000
- Cañameras, R., Yang, C., Nesvadba, N. P. H., et al. 2018, *A&A*, 620, A61
- Carilli, C., & Walter, F. 2013, *Annual Review of Astronomy and Astrophysics*, 51, 105
- Casey, C. M. 2016, *ApJ*, 824, 36
- Casey, C. M., Narayanan, D., & Cooray, A. 2014, *PhR*, 541, 45
- Casey, C. M., Berta, S., Béthermin, M., et al. 2012, *ApJ*, 761, 140
- Chabrier, G. 2003, *PASP*, 115, 763
- Chapman, S. C., Blain, A. W., Smail, I., & Ivison, R. J. 2005, *ApJ*, 622, 772
- Charlot, S., & Fall, S. M. 2000, *The Astrophysical Journal*, 539, 718
- Cicone, C., Maiolino, R., Sturm, E., et al. 2014, *A&A*, 562, A21
- Coil, A. L., Aird, J., Reddy, N., et al. 2015, *ApJ*, 801, 35
- Cunha, E., Walter, F., Smail, I. R., et al. 2015, *ApJ*, 806, 110
- Da Cunha, E., Charlot, S., & Elbaz, D. 2008, *Monthly Notices of the Royal Astronomical Society*, 388, 1595
- Daddi, E., Dannerbauer, H., Liu, D., et al. 2015, *A&A*, 577, A46
- Davé, R., Finlator, K., Oppenheimer, B. D., et al. 2010, *Monthly Notices of the Royal Astronomical Society*, 404, 1355
- Decarli, R., Walter, F., Aravena, M., et al. 2016a, *The Astrophysical Journal*, 833, 69
- . 2016b, *The Astrophysical Journal*, 833, 70
- Doherty, M. J., Geach, J. E., Ivison, R. J., & Dye, S. 2020, *ApJ*, 905, 152
- Elbaz, D., Dickinson, M., Hwang, H. S., et al. 2011, *A&A*, 533, A119
- Enia, A., Negrello, M., Gurwell, M., et al. 2018, *MNRAS*, 475, 3467
- Fixsen, D. J., Bennett, C. L., & Mather, J. C. 1999, *The Astrophysical Journal*, 526, 207
- Förster Schreiber, N. M., Genzel, R., Newman, S. F., et al. 2014, *ApJ*, 787, 38
- Fu, H., Jullo, E., Cooray, A., et al. 2012, *ApJ*, 753, 134
- Geach, J. E., Ivison, R. J., Dye, S., & Oteo, I. 2018, *The Astrophysical Journal*, 866, L12
- Geach, J. E., More, A., Verma, A., et al. 2015, *MNRAS*, 452, 502
- Genzel, R., Tacconi, L. J., Gracia-Carpio, J., et al. 2010, *Monthly Notices of the Royal Astronomical Society*, 407, 2091
- Genzel, R., Newman, S., Jones, T., et al. 2011, *ApJ*, 733, 101
- Goldsmith, P. F. 2001, *ApJ*, 557, 736
- Harrington, K. C., Yun, M. S., Cybulski, R., et al. 2016, *MNRAS*, 458, 4383
- Harrington, K. C., Weiss, A., Yun, M. S., et al. 2021, *ApJ*, 908, 95
- Hayward, C. C., Kereš, D., Jonsson, P., et al. 2011, *The Astrophysical Journal*, 743, 159
- Ho, P. T. P., Moran, J. M., & Lo, K. Y. 2004, *ApJL*, 616, L1
- Hwang, H. S., Elbaz, D., Magdis, G., et al. 2010, *MNRAS*, 409, 75
- Ivison, R. J., Papadopoulos, P. P., Smail, I., et al. 2011a, *MNRAS*, 412, 1913
- . 2011b, *Monthly Notices of the Royal Astronomical Society*, 412, 1913
- Jiao, Q., Gao, Y., & Zhao, Y. 2021, *MNRAS*, 504, 2360
- Jiao, Q., Zhao, Y., Zhu, M., et al. 2017, *ApJL*, 840, L18
- Kennicutt, Robert C., J. 1998, *ApJ*, 498, 541
- Kriek, M., Shapley, A. E., Reddy, N. A., et al. 2015, *ApJS*, 218, 15
- Magdis, G. E., Elbaz, D., Hwang, H. S., et al. 2010, *MNRAS*, 409, 22
- Magnelli, B., Lutz, D., Santini, P., et al. 2012, *A&A*, 539, A155
- Magnelli, B., Lutz, D., Saintonge, A., et al. 2014, *A&A*, 561, A86
- Mashian, N., Sturm, E., Sternberg, A., et al. 2015, *The Astrophysical Journal*, 802, 81
- Menéndez-Delmestre, K., Blain, A. W., Swinbank, M., et al. 2013, *ApJ*, 767, 151
- Nayyeri, H., Keele, M., Cooray, A., et al. 2016, *The Astrophysical Journal*, 823, 17
- Negrello, M., Perrotta, F., González-Nuevo, J., et al. 2007, *MNRAS*, 377, 1557
- Negrello, M., Hopwood, R., De Zotti, G., et al. 2010, *Science*, 330, 800
- Negrello, M., Amber, S., Amvrosiadis, A., et al. 2017, *MNRAS*, 465, 3558
- Papadopoulos, P. P., van der Werf, P. P., Xilouris, E. M., et al. 2012, *Monthly Notices of the Royal Astronomical Society*, 426, 2601
- Peng, C. Y., Ho, L. C., Impey, C. D., & Rix, H.-W. 2010, *AJ*, 139, 2097

- Riechers, D. A., Cooray, A., Pérez-Fournon, I., & Neri, R. 2021, *ApJ*, 913, 141
- Riechers, D. A., Bradford, C. M., Clements, D. L., et al. 2013, *Nature*, 496, 329
- Rosenberg, M. J. F., van der Werf, P. P., Aalto, S., et al. 2015, *ApJ*, 801, 72
- Saintonge, A., Kauffmann, G., Wang, J., et al. 2011, *Monthly Notices of the Royal Astronomical Society*, 415, 61
- Saintonge, A., Lutz, D., Genzel, R., et al. 2013, *ApJ*, 778, 2
- Sargent, M. T., Daddi, E., Béthermin, M., et al. 2014, *The Astrophysical Journal*, 793, 19
- Schöier, F. L., van der Tak, F. F. S., van Dishoeck, E. F., & Black, J. H. 2005, *A&A*, 432, 369
- Scoville, N., Aussel, H., Sheth, K., et al. 2014, *ApJ*, 783, 84
- Serjeant, S. 2012, *MNRAS*, 424, 2429
- Shapley, A. E., Reddy, N. A., Kriek, M., et al. 2015, *ApJ*, 801, 88
- Speagle, J. S., Steinhardt, C. L., Capak, P. L., & Silverman, J. D. 2014, *ApJS*, 214, 15
- Spilker, J. S., Marrone, D. P., Aguirre, J. E., et al. 2014, *The Astrophysical Journal*, 785, 149
- Sturm, E., González-Alfonso, E., Veilleux, S., et al. 2011, *ApJL*, 733, L16
- Su, T., Marriage, T. A., Asboth, V., et al. 2017, *MNRAS*, 464, 968
- Swinbank, A. M., Papadopoulos, P. P., Cox, P., et al. 2011, *ApJ*, 742, 11
- Symeonidis, M., Vaccari, M., Berta, S., et al. 2013, *Monthly Notices of the Royal Astronomical Society*, 431, 2317
- Tacconi, L. J., Neri, R., Genzel, R., et al. 2013, *ApJ*, 768, 74
- Timmons, N., Cooray, A., Nayyeri, H., et al. 2015, *ApJ*, 805, 140
- Toft, S., Smolčić, V., Magnelli, B., et al. 2014, *ApJ*, 782, 68
- Tunnard, R., & Greve, T. R. 2016, *ApJ*, 819, 161
- van der Tak, F. F. S., Black, J. H., Schöier, F. L., Jansen, D. J., & van Dishoeck, E. F. 2007, *A&A*, 468, 627
- Viero, M. P., Asboth, V., Roseboom, I. G., et al. 2014, *ApJS*, 210, 22
- Wardlow, J. L., Cooray, A., De Bernardis, F., et al. 2013, *ApJ*, 762, 59
- Weiß, A., Henkel, C., Downes, D., & Walter, F. 2003, *A&A*, 409, L41
- Yang, C., Omont, A., Beelen, A., et al. 2017, *A&A*, 608, A144